ADVANCED ENERGY MATERIALS
www.advenergymat.de

Li-Doping and Pyrolysis Engineered Robust Anode for Intermittency-Resilient AEM Electrolysis

Linchuan Cong, Cheng Tang, Xinxin Li, Wenjun He, Changli Wang, Eugenia Angelica, and Qiang Zhang**

The future of green hydrogen production via anion exchange membrane (AEM) water electrolysis lies in its integration with fluctuating renewable energy sources. However, the intermittent nature of renewables imposes stringent demands on the dynamic stability of highly active electrodes. To resolve this trade-off between activity and stability of nickel-based catalysts, this contribution describes a Li-doping strategy coupled with pyrolysis to engineer a self-supported nickel-iron-cobalt-lithium oxide anode on nickel felt. Pyrolysis yields a dense, crystalline oxide lattice that is firmly anchored to the substrate, while Li incorporation induces lattice contraction and reinforces metal–oxygen bonds, significantly suppressing active metal dissolution. Simultaneously, Li-driven electronic-structure modulation enhances charge transfer and accelerates pre-oxidation, collectively boosting oxygen evolution kinetics. The electrode achieves a low overpotential of 293 mV at 100 mA cm^{-2}, endures 500 h of steady-state operation at 500 mA cm^{-2} with negligible decay, and demonstrates exceptional resilience under simulated power fluctuations. In a custom AEM electrolyzer, it delivers a high current density of 2000 mA cm^{-2} at 1.90 V, exhibits a low degradation rate of 0.09 mV h^{-1} at 1000 mA cm^{-2}, and withstands 100 h of 60 s start/stop operation (3000 cycles). This work offers a compelling pathway to accelerate the development of green hydrogen by engineering electrodes that combine favorable activity with robust durability, enabling seamless integration with cost-effective, intermittent renewable energy sources.

1. Introduction

As the global energy landscape rapidly transitions toward renewable sources, hydrogen has emerged as a strategic zero-carbon energy carrier.[1,2] Anion exchange membrane water electrolysis (AEMWE) is recognized as a promising platform for scalable green hydrogen production owing to its high energy efficiency, low reliance on noble metals, and excellent compatibility with intermittent renewables such as wind and solar power.[3–5] However, the intrinsic intermittency and severe fluctuations of renewable power impose unprecedented challenges on electrocatalyst design.[6,7] Electrodes must exhibit not only outstanding catalytic activity to reduce energy consumption but also exceptional structural durability under harsh dynamic operating conditions—including high current densities, frequent start/stop cycles, and rapid load changes.[8] This dual demand for high activity and robust stability remains a critical bottleneck in the efficient integration of AEMWE with fluctuating renewable energy.

Currently, nickel-based materials are the most widely adopted oxygen evolution reaction (OER) electrocatalysts at AEMWE anodes owing to their low cost and high catalytic activity.[9–11] However, conventional Ni-based systems face significant limitations under practical dynamic conditions. On one hand, highly active compositions such as NiFe layered double hydroxides suffer from obvious degradation via active species dissolution and phase transformations,[12–14] especially under non-steady-state operation.[15,16] On the other hand, thermally pyrolyzed oxides (e.g., $NiCoO_x$) offer improved structural robustness but often display insufficient activity due to reduced active site exposure and compromised conductivity.[17–20] Therefore, a key challenge lies in enhancing the intrinsic catalytic activity of structurally stable pyrolyzed materials without sacrificing their durability for resolving dynamic operational adaptability.

Electrocatalytic performance can be rationally tailored by a variety of strategies, including defect engineering,[21–24] heteroatom doping,[25–28] strain modulation,[29–32] facet control,[33–35] and interface design.[36–39] Among these, heteroatom doping has proven effective to modulate both the electronic structure and lattice stability of materials. Lithium, in particular, offers a unique synergistic functionality: i) lower-valent Li^+ substitution generates a strong inductive effect that stabilizes

L. Cong, C. Tang, X. Li, W. He, C. Wang, E. Angelica, Q. Zhang
Tsinghua Center for Green Chemical Engineering Electrification
Department of Chemical Engineering
Tsinghua University
Beijing 100084, P. R. China
E-mail: cheng-net0@tsinghua.edu.cn;
zhang-qiang@mails.tsinghua.edu.cn
C. Tang, Q. Zhang
State Key Laboratory of Chemical Engineering and Low-Carbon Technology
Tsinghua University
Beijing 100084, P. R. China
C. Tang
Ordos Laboratory
Inner Mongolia 017000, P. R. China

The ORCID identification number(s) for the author(s) of this article can be found under https://doi.org/10.1002/aenm.202504707

DOI: 10.1002/aenm.202504707

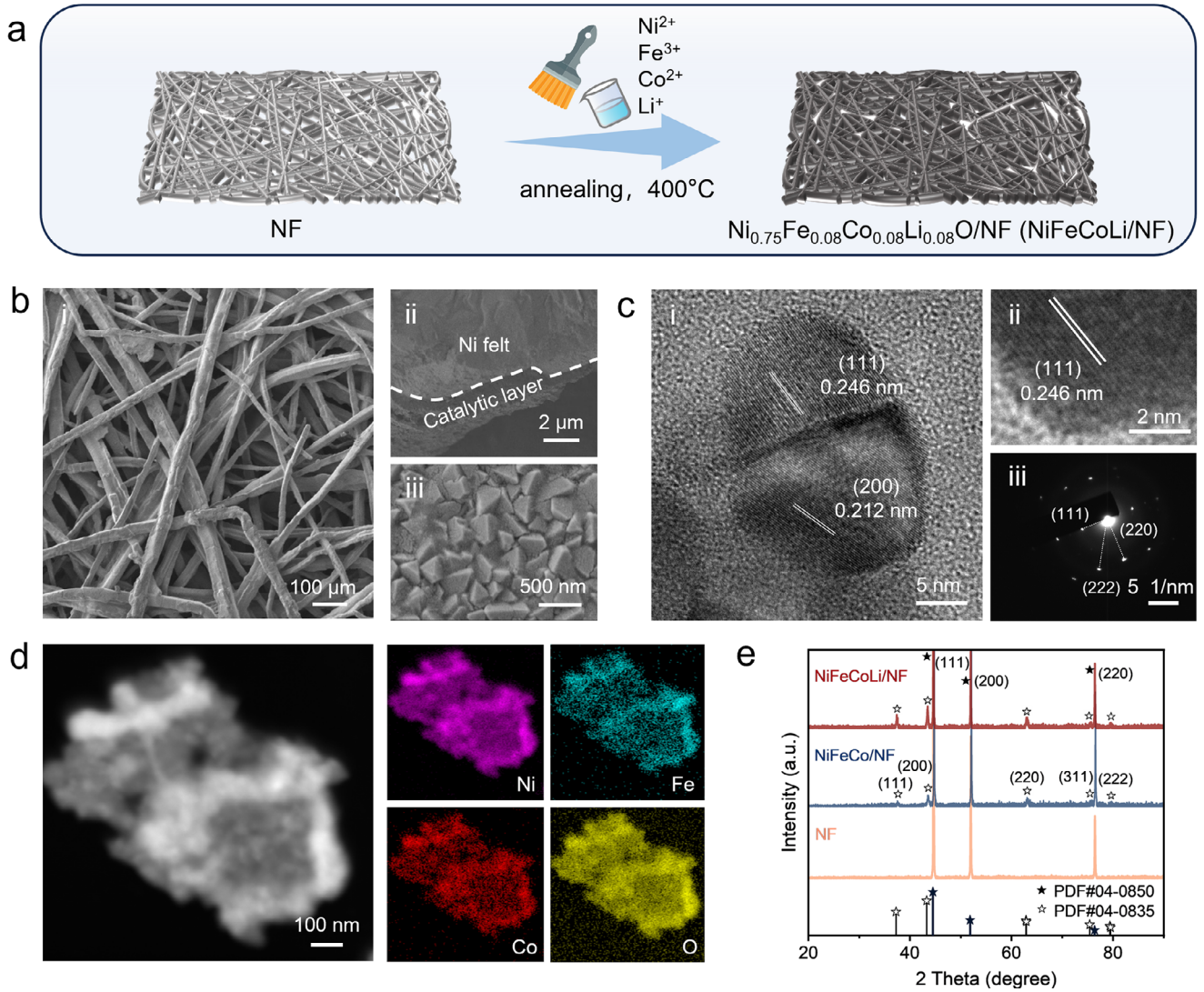

Figure 1. Materials synthesis and morphology characterizations. a) Schematic of the synthesis process of NiFeCoLi/NF. b) SEM images of NiFeCoLi/NF: i) low-resolution SEM image, ii) cross-sectional SEM image, and iii) high-resolution top-view SEM image. c) TEM images and selected area electron diffraction (SAED) pattern of NiFeCoLi/NF: i) and ii) high-resolution TEM images, and iii) SAED pattern. d) HAADF-STEM image and corresponding EDS mapping of Ni, Fe, Co and O elements for NiFeCoLi/NF. e) XRD patterns of NiFeCoLi/NF, NiFeCo/NF, and NF.

high-valence transition-metal centers to boost reaction activity, ii) the resultant mixed-valence states and newly formed conductive channels markedly reduce interfacial charge-transfer resistance and improve electrical conductivity, and iii) the atomic-radius mismatch induces lattice strain or chemical pressure,[40,41] which tunes intermediate adsorption energies and thereby accelerates reaction kinetics. These combined benefits have been validated in diverse systems, such as Li-doped high-entropy oxides for enhanced conductivity,[42] Li-intercalated IrO_x for improved acidic OER performance,[43] and surface-doped SnLi alloys for boosted CO_2 reduction.[44] Yet, the use of Li doping to optimize the activity–stability balance in pyrolyzed oxide catalysts under the dynamic, intermittent characteristic of AEMWE remains largely unexplored, and a mechanistic understanding of the underlying lattice–electronic interplay is still lacking.

In this contribution, we describe a Li-doped nickel-iron-cobalt oxide anode self-supported on nickel felt (NiFeCoLi/NF) fabricated via pyrolysis, which integrates structural stability and high catalytic activity for AEMWE. We demonstrate that Li incorporation significantly reduces OER overpotentials and accelerates reaction kinetics. The underlying enhancement mechanism is elucidated by comprehensive spectroscopy characterizations. More importantly, NiFeCoLi/NF exhibits excellent operational durability, showing negligible performance degradation over 500 h at 500 mA cm^{-2}. Under simulated intermittent power conditions mimicking renewable energy fluctuations, the electrode maintains superior stability, confirming its dynamic adaptability. This work establishes a rational design strategy for activity–stability synergy in pyrolyzed oxide catalysts, providing a foundation for the future development of fluctuation-resilient electrochemical systems.

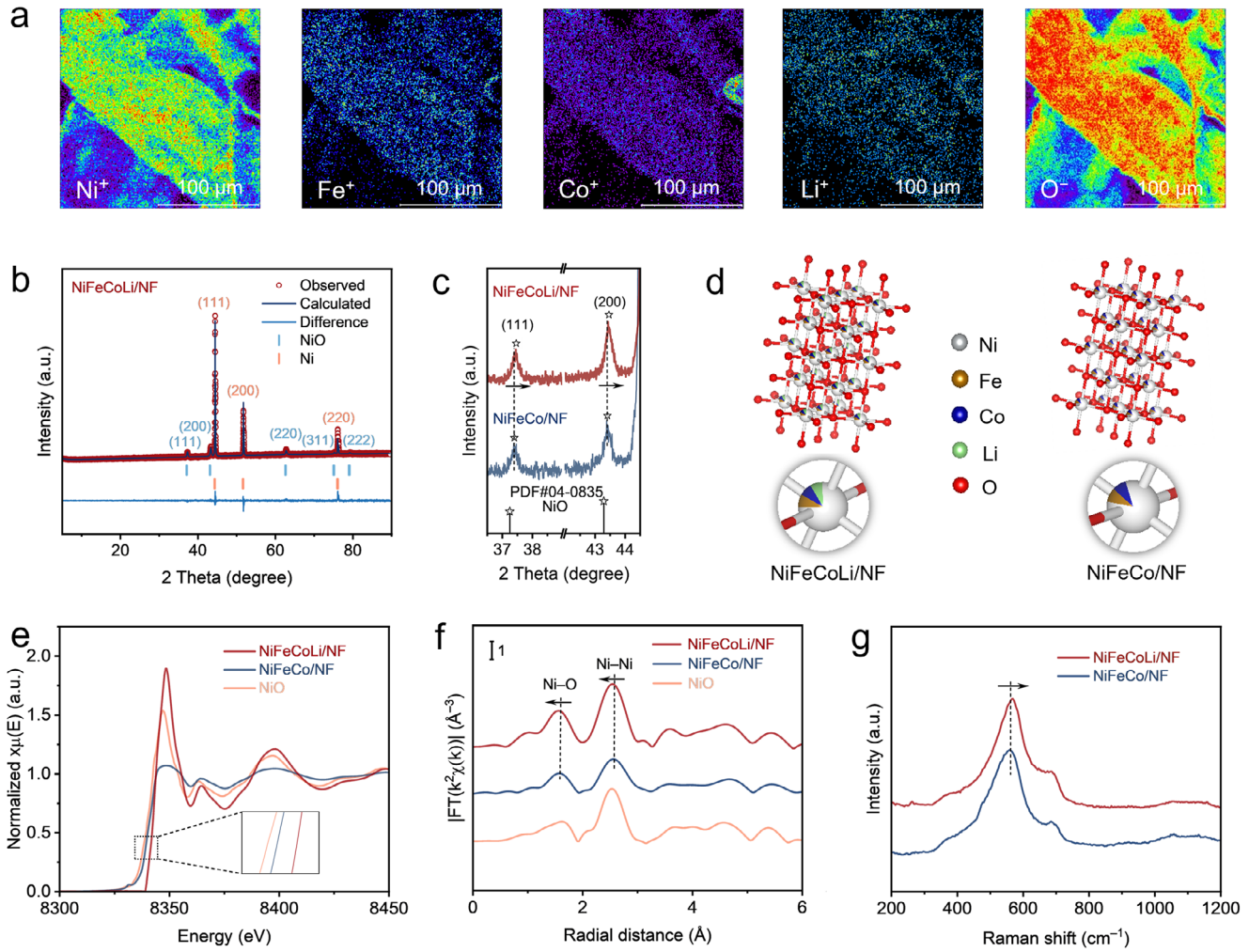

Figure 2. Structural characterizations. a) TOF-SIMS images of the selected region of NiFeCoLi/NF. b) Rietveld refinement of the XRD pattern of NiFeCoLi/NF. c) Enlarged XRD patterns and d) crystal structure of NiFeCoLi/NF and NiFeCo/NF. e) Normalized Ni K-edge XANES, and f) corresponding Ni K-edge FT-EXAFS spectra in *R* space of NiFeCoLi/NF, NiFeCo/NF and NiO. g) Raman spectra of NiFeCoLi/NF and NiFeCo/NF.

2. Results and Discussion

2.1. Materials Synthesis and Characterization

The intrinsic structural stability of NiFeCoLi/NF arises from a high-temperature pyrolysis treatment that promotes atomic rearrangement and generates a dense, defect-minimized lattice capable of withstanding the mechanical stress imposed by high potentials and current densities during AEMWE. As illustrated in **Figure** 1a, NiFeCoLi/NF was prepared by brush-coating nickel felt (NF) with a mixed precursor solution containing $Ni(NO_3)_2$, $Fe(NO_3)_3$, $Co(NO_3)_2$, and $LiNO_3$, followed by repeated pyrolysis cycles at 400°C in air. The mole ratio of Ni:Fe:Co:Li was 9:1:1:1. During each cycle, metal nitrates decompose to form oxides, which then chemically bond to the NF substrate, yielding a self-supported, multi-metal oxide coating layer (NiFeCoLi/NF). For comparison, NiFeCo/NF was synthesized identically but omitting $LiNO_3$ in the precursor solution. Scanning electron microscopy (SEM) images show that both NiFeCoLi/NF and NiFeCo/NF retain the open, 3D network of the nickel felt, enabling efficient electrolyte access and gas release (Figure 1b; Figure S1, Supporting Information). Energy-dispersive X-ray spectroscopy (EDS) mapping demonstrates uniform distributions of Ni, Fe, Co, and O across the coating for both samples, indicating complete and homogeneous oxide formation (Figure S2, Supporting Information). Cross-sectional SEM image shows a uniform ≈2 μm oxide layer seamlessly bonded to Ni fibers, ensuring mechanical integrity under harsh dynamic loads. High-resolution SEM image shows a densely packed, faceted 200–500 nm polygonal nanocrystals, exposing abundant active edge sites for enhanced OER. The surface morphology of undoped NiFeCo/NF is virtually identical, confirming that Li incorporation does not induce macroscopic morphological changes. The transmission electron microscopy (TEM) image shows well-defined lattice fringes in the NiFeCoLi/NF coating, with spacings of 0.212 and 0.246 nm corresponding to the (200) and (111) planes of NiO, respectively (Figure 1c). By comparison, NiFeCo/NF exhibits slightly larger spacings of 0.218 and 0.252 nm (Figure S3, Supporting Information), indicating that Li doping induces subtle lattice contraction.

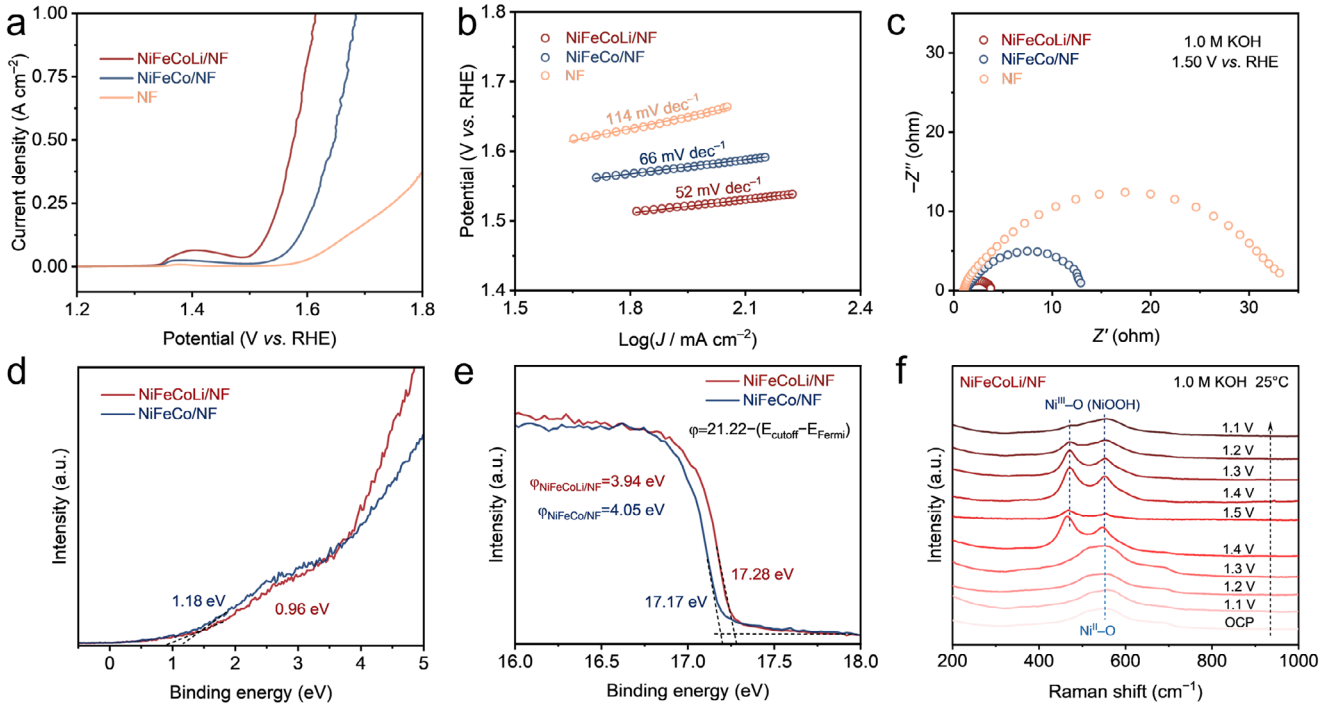

Figure 3. Electrocatalytic activity evaluation. a) LSV polarization curves, and b) corresponding Tafel plots of NiFeCoLi/NF, NiFeCo/NF and NF for OER. *J* is the current density. c) EIS Nyquist plots of NiFeCoLi/NF, NiFeCo/NF and NF obtained at 1.50 V vs. RHE. d) UPS investigations for the valence-band maximum and e) work function. f) In situ Raman spectra obtained in 1.0 M KOH for NiFeCoLi/NF.

High-angle annular dark-field scanning transmission electron microscopy (HAADF-STEM) and EDS mapping corroborate the homogeneous distributions of Ni, Fe, Co, and O (Figure 1d). X-ray diffraction (XRD) patterns for both samples are dominated by peaks indexed to NiO (PDF#04-0835) (Figure 1e), consistent with the TEM observations. Importantly, no new phases emerge upon Li doping, confirming that the original oxide lattice is preserved.

Time-of-flight secondary ion mass spectrometry (TOF-SIMS) mapping confirms a uniform distribution of Li^+ ions alongside other metal ions across the NiFeCoLi/NF surface, demonstrating homogeneous Li incorporation without phase segregation (**Figure** 2a). Rietveld refinement of XRD patterns for NiFeCoLi/NF versus NiFeCo/NF (Figure 2b; Figure S4, Supporting Information) reveals that Li doping contracts the unit-cell volume from 74.34 to 74.00 Å^3 (Table S1, Supporting Information), and shortens the average Ni—O bond from 2.102 to 2.099 Å (Table S2, Supporting Information). A slight shift of XRD patterns to larger 2θ provides further proof of lattice contraction (Figure 2c), while refined atomic ratios match precursor stoichiometry (Figure 2d; Table S3, Supporting Information). X-ray absorption spectroscopy (XAS) further elucidates the electronic modulation effect induced by Li doping. As shown in Figure 2e, Ni K-edge X-ray absorption near-edge structure (XANES) shifts to higher energy in NiFeCoLi/NF compared to NiFeCo/NF and NiO, indicating an elevated average Ni oxidation state. Fourier-transform extended X-ray absorption fine structure (FT-EXAFS) shows Ni—O and Ni—Ni peaks moving to shorter radial distances upon Li doping (Figure 2f). X-ray photoelectron spectroscopy (XPS) survey spectra confirm all constituent elements (Figure S5a, Supporting Information), and the high-resolution Ni 2p spectrum shifts to higher binding energy after Li incorporation, corroborating the XANES-derived increase in Ni valence (Figure S5b, Supporting Information). Raman spectra display a blue shift of the Ni–O vibration (≈550 cm^{-1}) in NiFeCoLi/NF (Figure 2g), which is attributed to the enhanced bond strength and altered electronic environment.

Taken together, the combination of high-temperature pyrolysis and Li doping yields a dense, strongly adherent multi-metal oxide layer with finely tuned lattice parameters. The hierarchical architecture endows NiFeCoLi/NF with outstanding mechanical integrity and electrochemical robustness, enabling it to withstand the dynamic stress of intermittent renewable power. The Li incorporation induces compressive strain that reinforces metal–oxygen covalency, optimizes the electronic structure, stabilizes active sites against dissolution and phase transformation, and ultimately confers high activity and durability under fluctuating electrolysis conditions.

2.2. Electrocatalytic Activity and Enhancement Mechanism

The electrocatalytic activity was evaluated in 1.0 M KOH electrolyte using the self-supported sample directly as the anode. Linear sweep voltammetry (LSV) curves show that NiFeCoLi/NF delivers 100 and 1000 mA cm^{-2} at overpotentials of 293 and 384 mV, respectively (**Figure** 3a; Figure S6, Supporting Information). These values are significantly lower than those of NiFeCo/NF (350 and 455 mV), and also lower than those of many other transition metal-based OER catalysts (Table S4, Supporting

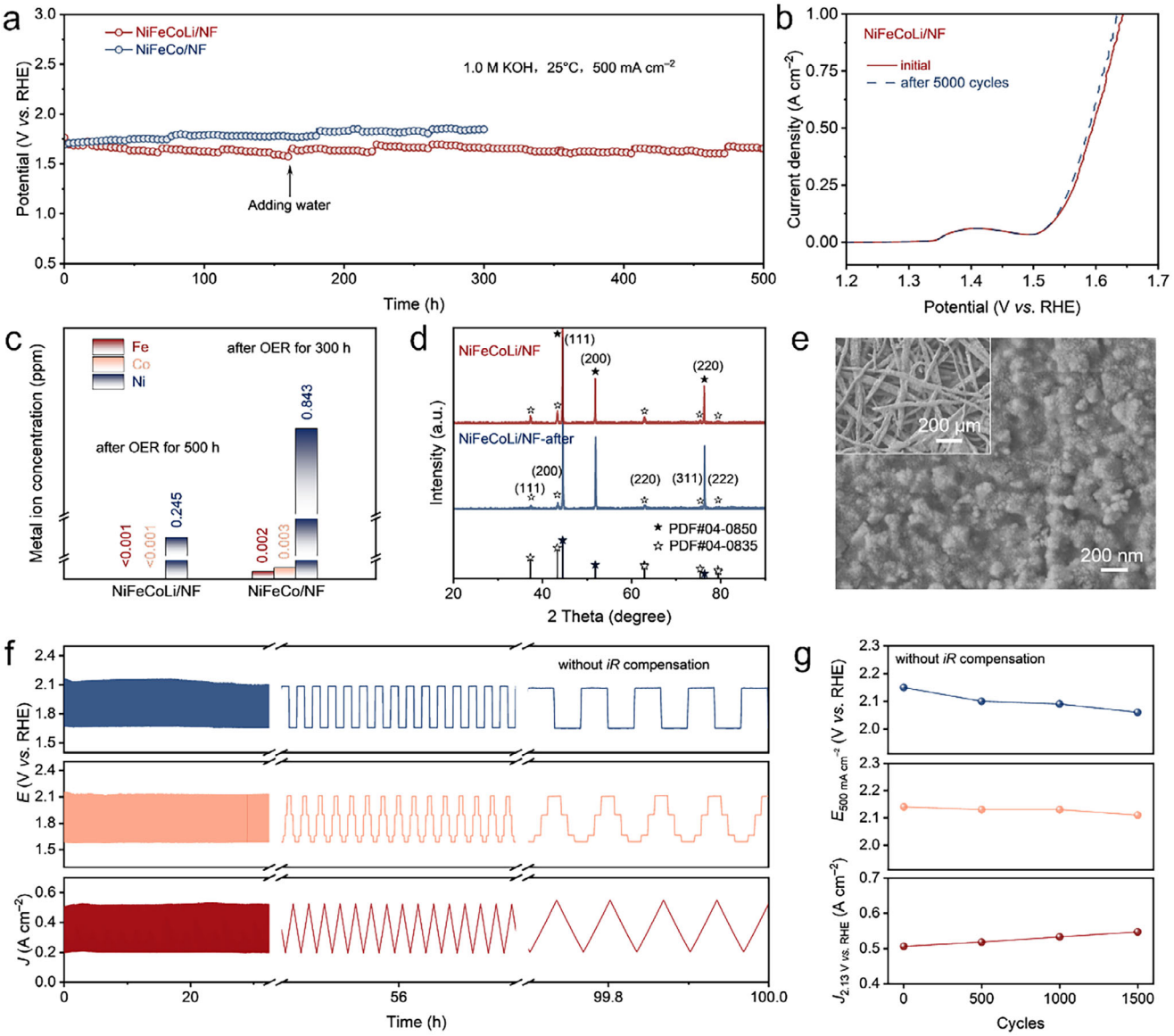

Figure 4. Electrocatalytic stability performance. a) Long-term stability test showing voltage profile at a constant current density of 500 mA cm^{-2} for 500 h. b) LSV polarization curves of NiFeCoLi/NF before and after 5000 LSV cycles. c) Ion dissolution characteristics measured by ICP-MS after OER stability tests for 300 or 500 h. d) XRD patterns of NiFeCoLi/NF before and after OER electrolysis for 500 h. e) SEM images of NiFeCoLi/NF after OER electrolysis for 500 h. f) Voltage/current responses to designed fluctuating input, and g) corresponding time-dependent characteristics for OER of NiFeCoLi/NF. *E* is the measured potential without *iR* compensation.

Information). The corresponding Tafel slope decreases from 66 to 52 mV dec^{-1} (Figure 3b), indicating accelerated rate-determining kinetics upon Li incorporation. Electrochemical impedance spectroscopy (EIS) reveals that the charge-transfer resistance (R_{ct}) of NiFeCoLi/NF is substantially lower than that of NiFeCo/NF and NF (Figure 3c; Figure S7, Supporting Information). Meanwhile, the double-layer capacitance (C_{dl}), a proxy for electrochemically active surface area, increases from 36.4 to 40.7 mF cm^{-2} (Figure S8, Supporting Information), indicating increased accessible active sites upon Li doping.

The activity enhancement mechanism was elucidated by comprehensive spectroscopy characterizations. UV–vis diffuse reflectance spectra (DRS) and Tauc-plot analysis reveal a band-gap narrowing from 3.04 to 2.55 eV after Li doping (Figure S9, Supporting Information), reflecting either an upward shift of the valence-band maximum or the introduction of Li-induced electronic states near the Fermi level, which lowers the energy barrier for electron excitation.[45,46] Complementary ultraviolet photoelectron spectroscopy (UPS) confirms the valence-band maximum shifting from 1.18 to 0.96 eV below the Fermi level (Figure 3d), while the work function (φ) decreases from 4.05 to 3.94 eV (Figure 3e). These results corroborate the enhanced electrical conductivity observed by EIS and support faster charge transfer during OER. In situ Raman spectroscopy was performed to track the structural evolution of the catalyst during OER (Figure 3f; Figure S10, Supporting Information). Upon

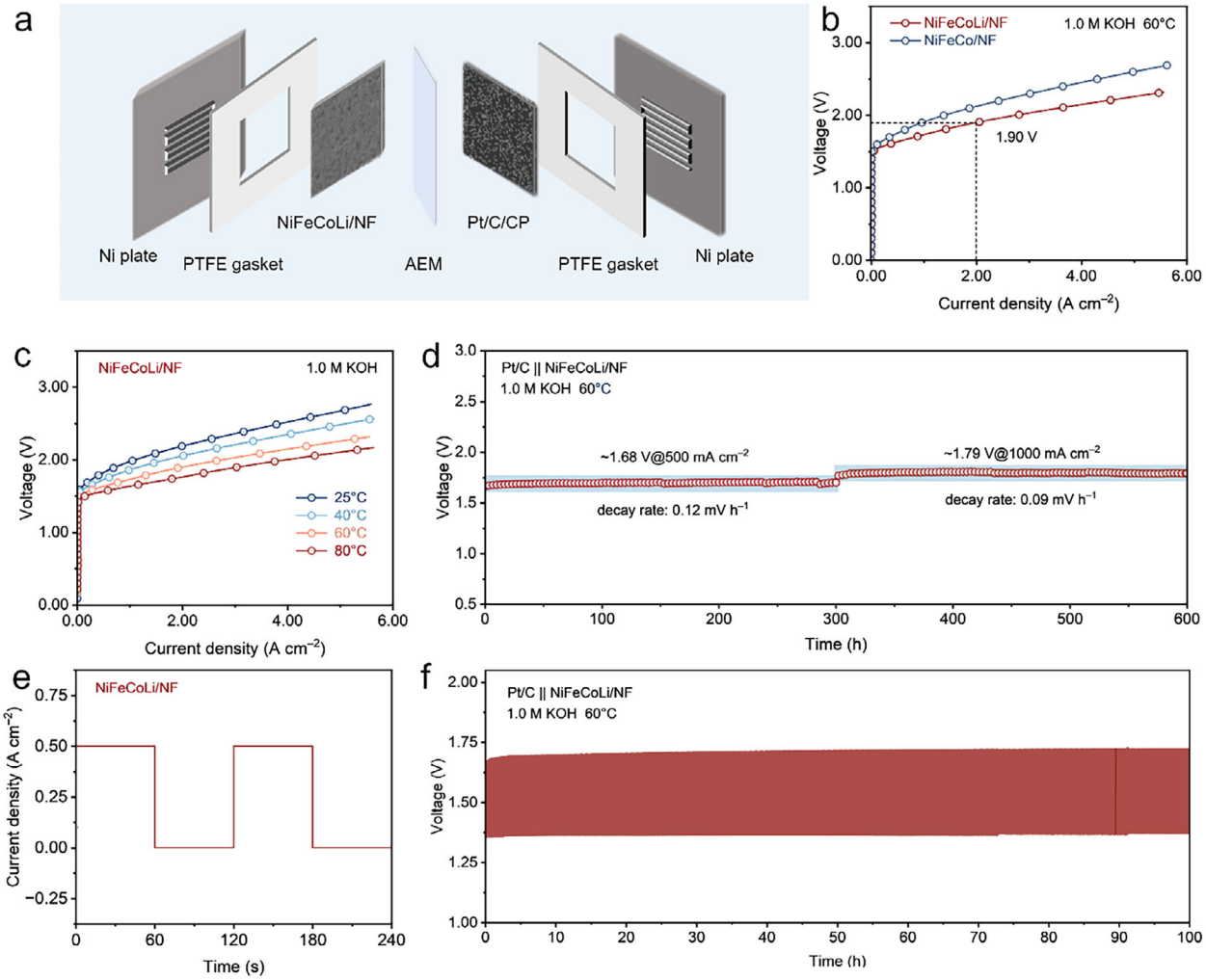

Figure 5. AEM electrolyzer performance evaluation. a) Exploded view of the custom AEM electrolyzer. b) Polarization curves of NiFeCoLi/NF and NiFeCo/NF for AEMWE in 1.0 M KOH at 60°C. c) Polarization curves for AEMWE at different temperatures in 1.0 M KOH. d) Long-term stability test at 500 and 1000 mA cm^{-2} for AEMWE. e) Simulated input and f) corresponding output of start/stop operation of AEM electrolyzer.

applying a potential higher than 1.40 V vs. reversible hydrogen electrode (RHE), the Ni^{2+}–O band (≈560 cm^{-1}) corresponding to oxides gradually disappears, while the Ni^{3+}–O signatures (≈480 and ≈560 cm^{-1}) assigned to NiOOH phase emerge.[47,48] It is noteworthy that NiFeCoLi/NF exhibits the NiOOH transition ≈50 mV earlier than NiFeCo/NF, evidencing a lower activation barrier for the precatalytic transformation.

Collectively, Li doping not only tunes the oxide's lattice parameters but also optimizes its electronic structures to elevate Ni valence, enhance electrical conductivity, accelerate active-phase formation, and improve charge transfer, synergistically boosting intrinsic OER activity of the pyrolyzed metal oxides.

2.3. Steady and Dynamic Durability

The long-term steady-state stability of NiFeCoLi/NF and NiFeCo/NF was evaluated at 500 mA cm^{-2} at room temperature in 1.0 M KOH (**Figure** 4a). NiFeCoLi/NF exhibits negligible potential decay over 500 h, whereas NiFeCo/NF suffers >100 mV degradation within 300 h. After 5000 LSV (0.80–1.60 V vs. RHE), NiFeCoLi/NF shows no loss of activity but even a slight increase (Figure 4b), potentially attributed to the electrochemical activation. Inductively coupled plasma mass spectrometry (ICP-MS) analysis quantifies only 0.245 ppm Ni leaching from NiFeCoLi/NF in 500 h electrolysis versus 0.843 ppm from NiFeCo/NF in 300-h electrolysis (Figure 4c), confirming that Li-induced lattice contraction suppresses metal dissolution. Post-mortem XRD analysis (Figure 4d; Figure S11, Supporting Information) and SEM images (Figure 4e) demonstrate that both NiFeCoLi/NF and NiFeCo/NF retain the NiO phase and nanostructure after stability tests. High-resolution TEM images (Figure S12a–c, Supporting Information) and Raman spectroscopy (Figure S13, Supporting Information) reveal the formation of amorphous NiOOH surface, while EDS mapping (Figure S12d, Supporting Information) and XPS analysis (Figure S14, Supporting Information) confirm the uniform element

distribution and unchanged surface chemistry, evidencing robust phase integrity.

To validate the electrode adaptability to fluctuating renewable energy, several dynamic tests were designed (Figure S15, Supporting Information): square-wave current steps (between 100 and 500 mA cm^{-2}), staircase current ramp, and triangular voltage sweep. Through these tests, NiFeCoLi/NF responds rapidly with minimal potential/current oscillation (Figure 4f,g). Therefore, the as-fabricated NiFeCoLi/NF anode not only exhibits outstanding long-term stability under steady electrolysis conditions but also maintains stable performance under simulated renewable-power fluctuations, highlighting its dual resilience in both steady and dynamic electrolysis regimes. It should be noted that while the dynamic durability tests in this study demonstrate the catalyst's fundamental resilience to fluctuating operation, real renewable energy fluctuations can be more rapid and stochastic. Future work will focus on designing dynamic protocols that more closely mimic real-world scenarios to further evaluate their potential for industrial applications.

2.4. AEM Electrolyzer Performance

To assess the industrial viability, we assembled a custom AEMWE using NiFeCoLi/NF as the anode and carbon paper (CP) supported Pt/C as the cathode (**Figure 5a**). At 60°C in 1.0 M KOH, the cell delivers 2000 mA cm^{-2} at 1.90 V (Figure 5b), markedly outperforming both NiFeCo/NF and most oxide-based electrodes. The AEMWE performance exhibits notable temperature dependence: as the operating temperature rises from 25 to 80°C, the cell voltage at 1000 mA cm^{-2} decreases from 1.97 to 1.68 V, owing to enhanced electrolysis thermodynamics and accelerated ion transport (Figure 5c). Steady-state stability under industrial conditions was probed by continuous operation at 500 and 1000 mA cm^{-2} for 300 h each (Figure 5d). Voltage decay rates are as low as 0.12 and 0.09 mV h^{-1}, respectively, indicating exceptional stability at high current densities. To further evaluate the practical applicability under fluctuating renewable energy input, intermittent stability tests were performed with 60-s start/stop intervals (Figure 5e). Over 100-h start/stop cycling (3000 times), the electrode exhibits negligible performance degradation (Figure 5f), demonstrating robust tolerance to dynamic load profiles. The synergistic effect of the stable adherent oxide architecture constructed through pyrolysis and the Li-induced lattice contraction underpins the NiFeCoLi/NF electrode's superior durability in both steady-state and fluctuating AEMWE operations, rendering it ideally suited for integration with intermittent renewable energy sources.

3. Conclusion

Lithium doping was integrated with high-temperature pyrolysis to fabricate a multi-metal oxide anode on nickel felt, achieving both enhanced activity and dynamic stability. Pyrolysis produces a dense, strongly adherent interface that secures intrinsic mechanical robustness, while Li incorporation induces lattice contraction, fortifying metal–oxygen bonds and suppressing cation dissolution. Concurrently, Li-driven electronic-structure modulation elevates the Ni valence and accelerates charge transfer—lowering the OER energy barrier and affording a Tafel slope of just 52 mV dec^{-1}. The resulting NiFeCoLi/NF electrode delivers 100 mA cm^{-2} at 293 mV overpotential and exhibits zero decay over 500 h at 500 mA cm^{-2}. Under simulated wind/solar fluctuations, it responds rapidly and maintains stable performance. In a practical AEM electrolyzer, the anode achieves 2000 mA cm^{-2} at 1.90 V with an ultralow decay rate of 0.09 mV h^{-1} at 1000 mA cm^{-2}, surviving 3000 start/stop cycles. This synergistic approach overcomes the activity–stability trade-off in Ni-based OER catalysts and offers a design paradigm for electrolyzers tailored to intermittent renewable power through interface engineering and electronic modulation.

Supporting Information

Supporting Information is available from the Wiley Online Library or from the author.

Acknowledgements

The authors appreciate the support from the National Key Research and Development Program of China (2024YFE0211400, 2024YFB4006500), the State Grid Headquarter Science and Technology Project (5419-202399650A-3-2-ZN), the National Natural Science Foundation of China (22478221, 22521202), the China Postdoctoral Science Foundation (2025M771125, GZC20250767), the Huaneng Group Science and Technology Research Project (HNKJ23-H71), Ordos Laboratory, and Tsinghua University Initiative Scientific Research Program.

Conflict of Interest

The authors declare no conflict of interest.

Data Availability Statement

The data that support the findings of this study are available from the corresponding author upon reasonable request.

Keywords

anion exchange membrane water electrolysis, fluctuating renewable energy, lithium doping electrocatalyst, pyrolysis process, strain effect

Received: August 22, 2025
Revised: September 6, 2025
Published online:

[1] N. Johnson, M. Liebreich, D. M. Kammen, P. Ekins, R. McKenna, I. Staffell, *Nat. Rev. Clean Technol.* **2025**, *1*, 351.
[2] C. Tang, Q. Zhang, *Engineering* **2023**, *29*, 22.
[3] N. Du, C. Roy, R. Peach, M. Turnbull, S. Thiele, C. Bock, *Chem. Rev.* **2022**, *122*, 11830.
[4] Q. Li, A. M. Villarino, C. R. Peltier, A. J. Macbeth, Y. Yang, M.-J. Kim, Z. Shi, M. R. Krumov, C. Lei, G. G. Rodríguez-Calero, J. Soto, S.-H. Yu, P. F. Mutolo, L. Xiao, L. Zhuang, D. A. Muller, G. W. Coates, P. Zelenay, H. D. Abruña, *J. Phys. Chem. C* **2023**, *127*, 7901.
[5] S. Shaik, J. Kundu, Y. Yuan, W. Chung, D. Han, U. Lee, H. Huang, S. Choi, *Adv. Energy Mater.* **2024**, *14*, 2401956.

[6] S. F. Amireh, N. N. Heineman, P. Vermeulen, R. L. G. Barros, D. Yang, J. van der Schaaf, M. T. de Groot, *J. Power Sources* **2023**, *560*, 232629.
[7] X. Shi, Y. Qian, S. Yang, *ACS Sustain. Chem. Eng.* **2020**, *8*, 7097.
[8] H. Kojima, K. Nagasawa, N. Todoroki, Y. Ito, T. Matsui, R. Nakajima, *Int. J. Hydrogen. Energy* **2023**, *48*, 4572.
[9] W. Kuang, Z. Cui, C. Wang, T. Chen, Q. Wang, S. Li, T. Yang, J. Liu, *Adv. Energy Mater.* **2025**, *15*, 2406080.
[10] J. Fan, X. Xiang, Y. Liu, X. Yang, N. Shi, D. Xu, C. Zhou, M. Han, J. Bao, W. Huang, *Sus. Mat.* **2025**, *5*, 70010.
[11] Z. Xu, Z.-S. Wu, *eScience* **2025**, *5*, 100334.
[12] H. Liao, G. Ni, P. Tan, K. Liu, X. Liu, H. Liu, K. Chen, X. Zheng, M. Liu, J. Pan, *Adv. Mater.* **2023**, *35*, 2300347.
[13] N. Wang, S. Song, W. Wu, Z. Deng, C. Tang, *Adv. Energy Mater.* **2024**, *14*, 2303451.
[14] D. Y. Chung, P. P. Lopes, P. Farinazzo Bergamo Dias Martins, H. He, T. Kawaguchi, P. Zapol, H. You, D. Tripkovic, D. Strmcnik, Y. Zhu, S. Seifert, S. Lee, V. R. Stamenkovic, N. M. Markovic, *Nat. Energy* **2020**, *5*, 222.
[15] G. Wang, H. Li, F. Babbe, A. Tricker, E. J. Crumlin, J. Yano, R. Mukundan, X. Peng, *Adv. Energy Mater.* **2025**, *15*, 2500886.
[16] N. Guruprasad, J. van der Schaaf, M. T. de Groot, *J. Power Sources* **2024**, *613*, 234877.
[17] G. Shi, T. Tano, D. A. Tryk, M. Yamaguchi, A. Iiyama, M. Uchida, K. Iida, C. Arata, S. Watanabe, K. Kakinuma, *ACS Catal.* **2022**, *12*, 14209.
[18] N. Todoroki, K. Nagasawa, H. Enjoji, S. Mitsushima, *ACS Appl. Mater. Interfaces* **2023**, *15*, 24399.
[19] Y. Qu, M. M. Gomaa, M. H. Sayed, M. Boshta, G. Greczynski, R. Yakimova, J. Sun, *Adv. Mater. Interfaces* **2024**, *11*, 2300920.
[20] D. Clauss, V. Martin, J. Nelayah, R. Chattot, P. Bordet, J. Drnec, M. Mirolo, L. Dubau, F. Maillard, *ACS Catal.* **2025**, *15*, 2654.
[21] Y. Zhang, J. Liu, Y. Xu, C. Xie, S. Wang, X. Yao, *Chem. Soc. Rev.* **2024**, *53*, 10620.
[22] D. Yan, C. Xia, W. Zhang, Q. Hu, C. He, B. Xia, S. Wang, *Adv. Energy Mater.* **2022**, *12*, 2202317.
[23] P. Yan, M. Huang, B. Wang, Z. Wan, M. Qian, H. Yan, T. T. Isimjan, J. Tian, X. Yang, *J. Energy Chem.* **2020**, *47*, 299.
[24] Y. Luo, Y. Wu, C. Huang, C. Menon, S.-P. Feng, P. K. Chu, *EcoMat* **2022**, *4*, 12197.
[25] X. Li, C. Deng, Y. Kong, Q. Huo, L. Mi, J. Sun, J. Cao, J. Shao, X. Chen, W. Zhou, M. Lv, X. Chai, H. Yang, Q. Hu, C. He, *Angew. Chem., Int. Ed.* **2023**, *62*, 202309732.
[26] Y. Zhang, T. Wang, L. Mei, R. Yang, W. Guo, H. Li, Z. Zeng, *Nano-Micro Lett.* **2024**, *16*, 180.
[27] A. Gaur, J. Sharma, E. Enkhbayar, M. S. Cho, J. H. Ryu, H. Han, *Eco. Mat.* **2024**, *6*, 12484.
[28] A. Zhang, Y. Liang, H. Zhang, Z. Geng, J. Zeng, *Chem. Soc. Rev.* **2021**, *50*, 9817.
[29] M. Luo, S. Guo, *Nat. Rev. Mater.* **2017**, *2*, 17059.
[30] Y. Yan, J. Lin, K. Huang, X. Zheng, L. Qiao, S. Liu, J. Cao, S. C. Jun, Y. Yamauchi, J. Qi, *J. Am. Chem. Soc.* **2023**, *145*, 24218.
[31] H. Guo, S. Guo, *CCS Chem.* **2025**, *7*, 326.
[32] Z. Feng, C. Dai, Z. Zhang, X. Lei, W. Mu, R. Guo, X. Liu, J. You, *J. Energy Chem.* **2024**, *93*, 322.
[33] C. Wang, Q. Zhang, B. Yan, B. You, J. Zheng, L. Feng, C. Zhang, S. Jiang, W. Chen, S. He, *Nano-Micro Lett.* **2023**, *15*, 52.
[34] Y. Yao, G. Zhao, X. Guo, P. Xiong, Z. Xu, L. Zhang, C. Chen, C. Xu, T.-S. Wu, Y.-L. Soo, Z. Cui, M. M.-J. Li, Y. Zhu, *J. Am. Chem. Soc.* **2024**, *146*, 15219.
[35] Z. Liu, H. M. Amin, Y. Peng, M. Corva, R. Pentcheva, K. Tschulik, *Adv. Funct. Mater.* **2023**, *33*, 2210945.
[36] B. Jia, B. Zhang, Z. Cai, X. Yang, L. Li, L. Guo, *eScience* **2023**, *3*, 100112.
[37] H. Zhao, Z.-Y. Yuan, *J. Energy Chem.* **2021**, *54*, 89.
[38] R.-Y. Fan, J.-Y. Xie, N. Yu, Y.-M. Chai, B. Dong, *Int. J. Hydrogen. Energy* **2022**, *47*, 10547.
[39] L. Du, L. Xing, G. Zhang, X. Liu, D. Rawach, S. Sun, *SusMat* **2021**, *1*, 150.
[40] R. B. Wexler, J. M. P. Martirez, A. M. Rappe, *J. Am. Chem. Soc.* **2018**, *140*, 4678.
[41] Z. Fan, Y. Wang, Z. Leng, G. Gao, L. Li, L. Huang, G. Li, *J. Am. Chem. Soc.* **2024**, *146*, 11500.
[42] M. Song, X. Zhang, S. Wan, G. Wang, J. Liu, W. Li, H. Dong, C. Lou, Z. Chen, B. Chen, H. Zhang, *JACS Au* **2024**, *4*, 592.
[43] J. R. Esquius, D. J. Morgan, G. A. Siller, D. Gianolio, M. Aramini, L. Lahn, O. Kasian, S. A. Kondrat, R. Schlögl, G. J. Hutchings, R. Arrigo, S. J. Freakley, *J. Am. Chem. Soc.* **2023**, *145*, 6398.
[44] S. Yan, C. Peng, C. Yang, Y. Chen, J. Zhang, A. Guan, X. Lv, H. Wang, Z. Wang, T. K. Sham, Q. Han, G. Zheng, *Angew. Chem., Int. Ed.* **2021**, *60*, 25741.
[45] W. Ni, A. Krammer, C. S. Hsu, H. M. Chen, A. Schüler, X. Hu, *Angew. Chem., Int. Ed.* **2019**, *58*, 7445.
[46] W. Wu, Y. Wang, S. Song, Z. Ge, C. Zhang, J. Huang, G. Xu, N. Wang, Y. Lu, Z. Deng, H. Duan, M. Liu, C. Tang, *Angew. Chem., Int. Ed.* **2025**, *64*, 202504972.
[47] R. Jena, V. Kashyap, R. Jana, T. Mandal, T. N. Das, F. A. Rahimi, S. Barman, D. Maity, R. Kumar, D. Bhattacharyya, A. Datta, T. K. Maji, *Angew. Chem., Int. Ed.* **2025**, 202510741.
[48] X. Qiang, Y. Yao, J. Yin, P. Da, Z. Mu, K. Shen, Y. Sun, Y. Zhang, P. Li, Z. Li, P. Xi, C.-H. Yan, *Angew. Chem., Int. Ed.* **2025**, *64*, 202424014.